Simultaneous multislice magnetic resonance fingerprinting with low-rank and subspace modeling

HHS Public Access

Author manuscript

Conf Proc IEEE Eng Med Biol Soc. Author manuscript; available in PMC 2018 April 11.

Published in final edited form as:

Conf Proc IEEE Eng Med Biol Soc. 2017 July ; 2017: 3264–3268. doi:10.1109/EMBC.2017.8037553.

SIMULTANEOUS MULTISLICE MAGNETIC RESONANCE FINGERPRINTING WITH LOW-RANK AND SUBSPACE MODELING

Bo Zhao[†], **Berkin Bilgic**[†], **Elfar Adalsteinsson**[‡], **Mark A. Griswold**[★], **Lawrence L. Wald**[†], and **Kawin Setsompop**[†]

[†]Athinoula A. Martinos Center for Biomedical Imaging, Massachusetts General Hospital and Harvard Medical School

[★]Department of Biomedical Engineering, Case Western Reserve University

[‡]Department of Electrical Engineering and Computer Science, Massachusetts Institute of Technology

Abstract

Magnetic resonance fingerprinting (MRF) is a new quantitative imaging paradigm that enables simultaneous acquisition of multiple magnetic resonance tissue parameters (e.g., T_1, T_2, and spin density). Recently, MRF has been integrated with simultaneous multislice (SMS) acquisitions to enable volumetric imaging with faster scan time. In this paper, we present a new image reconstruction method based on low-rank and subspace modeling for improved SMS-MRF. Here the low-rank model exploits strong spatiotemporal correlation among contrast-weighted images, while the subspace model captures the temporal evolution of magnetization dynamics. With the proposed model, the image reconstruction problem is formulated as a convex optimization problem, for which we develop an algorithm based on variable splitting and the alternating direction method of multipliers. The performance of the proposed method has been evaluated by numerical experiments, and the results demonstrate that the proposed method leads to improved accuracy over the conventional approach. Practically, the proposed method has a potential to allow for a 3x speedup with minimal reconstruction error, resulting in less than 5 sec imaging time per slice.

Index Terms

Low-rank model; subspace model; sparse sampling; simultaneous multislice (SMS); quantitative magnetic resonance imaging (qMRI)

1. INTRODUCTION

Most clinical magnetic resonance imaging (MRI) applications rely on contrast-weighted images, which are complex functions of intrinsic magnetic resonance (MR) tissue parameters (e.g., T_1, T_2, and spin density) and external scan settings (e.g., field inhomogeneity and coil geometry). These images are qualitative in nature, which provide limited capability for direct inter- and intra-patient comparisons across different institutions

and/or across scanners. Quantitative MRI is a promising direction to overcome these limitations [1]; but it often results in prolonged data acquisition time. Magnetic resonance fingerprinting (MRF) [2] is a very recent breakthrough in quantitative MRI, which enables rapid acquisition of multiple MR tissue parameters. For example, with MRF, the acquisition time can be shortened to around 15 sec for acquiring a single imaging slice.

Although MRF provides an unprecedented imaging speed, it could still result in clinically unacceptable lengthy acquisitions of up to 20 minutes for volumetric coverage of e.g., the brain with a large number of imaging slices. Simultaneous multislice (SMS) imaging [3–6] is a powerful data acquisition methodology, which enables rapid volumetric imaging through acquiring data from multiple imaging slices simultaneously rather than sequentially. Recently, SMS techniques have been integrated with MRF to improve the imaging speed for volumetric quantitative MRI [7–9]. For data acquisition, additional gradient blips along slice direction are added, which generate phase modulation for simultaneously acquired slices. For image reconstruction, [7] integrates the conventional approach with slice sensitivity encoding (SENSE) method, while [8] combines generalized autocalibrating partially parallel acquisition (GRAPPA) with slice-GRAPPA. A more recent approach generalizes the above methods by using different acquisition parameters (e.g., flip angle and RF phases) for each slice [9], which is able to achieve a number of desired properties (e.g., reduced peak RF amplitude, and signals between slices being more orthogonal).

Extending our early work in [10], this work presents a new image reconstruction method for SMS-MRF. It utilizes the low-rank and subspace modeling to enable accurate reconstruction of MR tissue parameter maps from highly-undersampled data. Here the low-rank model exploits strong spatiotemporal correlation among MRF contrast-weighted images, while the subspace model captures the temporal evolution of magnetic dynamics. The proposed model results in a convex optimization problem, which is solved by a numerical algorithm based on variable splitting (VS) [11–13] and the alternating direction method of multipliers [12–14]. The effectiveness of the proposed method was evaluated with numerical experiments.

2. PROPOSED APPROACH

2.1. Problem Formulation

Assuming that N_s imaging slices are simultaneously excited at the mth time instant [or repetition time (TR)], the imaging equation for SMS-MRF can be written as

$$\mathbf{d}_{m,c} = \mathbf{F}_m \sum_{q=1}^{N_s} \mathbf{S}_{c,q} \mathbf{I}_{m,q} + \mathbf{n}_{m,c}, \quad (1)$$

for $m = 1, \cdots, M$ and $c = 1, \cdots, N_c$, where $\mathbf{I}_{m,q} \in \mathbb{C}^N$ denotes the contrast-weighted image associated with the mth TR and qth slice, $\mathbf{S}_{c,q} \in \mathbb{C}^{N \times N}$ a diagonal matrix whose diagonal entries contain the coil sensitivity profile for the cth coil and qth slice, $\mathbf{F}_m \in \mathbb{C}^{P_m \times N}$ the undersampled Fourier encoding matrix for the mth time instant, $\mathbf{d}_{m,c} \in \mathbb{C}^{P_m}$ the measured **k**-space data, and $\mathbf{n}_{m,c} \in \mathbb{C}^{P_m}$ the measurement noise.

For simplicity, we consider a discrete image model, in which the contrast-weighted images associated with each slice can be represented by the following Casorati matrix [15], i.e.,

$$\mathbf{C}_q = \begin{bmatrix} \mathbf{I}_{1,q}(\mathbf{x}_1) & \cdots & \mathbf{I}_{M,q}(\mathbf{x}_1) \\ \vdots & \ddots & \vdots \\ \mathbf{I}_{1,q}(\mathbf{x}_N) & \cdots & \mathbf{I}_{M,q}(\mathbf{x}_N) \end{bmatrix} \in \mathbb{C}^{N \times M}.$$

With this notation, (1) can be rewritten as

$$\mathbf{d}_c = \Omega(\mathbf{F} \sum_{q=1}^{N_s} \mathbf{S}_{c,q} \mathbf{C}_q) + \mathbf{n}_c,$$

for $c = 1, \cdots, N_c$, where $\mathbf{d}_c$ and $\mathbf{n}_c$ are both $P \times 1$ ($P = \sum_{m=1}^{M} P_m$) complex vectors that respectively contain the measured data and measurement noise from all the time instants associated with the cth receiver coil, $\mathbf{F} \in \mathbb{C}^{\hat{N} \times N}$ denotes the fully-sampled Fourier encoding matrix, and $\Omega(\cdot) \in \mathbb{C}^{\hat{N} \times M} \rightarrow \mathbb{C}^P$ denotes the ($\mathbf{k}$, t)-space sparse sampling operator that acquires $\mathbf{k}$-space data from each TR and then concatenates the data into $\mathbf{d}_c$.

Given that there is strong spatiotemporal correlation among the contrast-weighted images, $\mathbf{C}_q$ admits a low-rank approximation. Invoking a low-rank constraint, the image reconstruction problem can be formulated as follows:

$$\left\{\widehat{\mathbf{C}}_q\right\}_{q=1}^{N_s} = \arg \min_{\{\mathbf{C}_q\}} \sum_{c=1}^{N_c} \left\| \mathbf{d}_c - \Omega(\mathbf{F} \sum_{q=1}^{N_s} \mathbf{S}_{c,q} \mathbf{C}_q) \right\|_2^2 + \sum_{q=1}^{N_s} R_r(\mathbf{C}_q),$$

where $R_r(\mathbf{C}_q)$ denotes a low-rank regularization functional. There are a number of ways of imposing a rank constraint. Here, we enforce an explicit low-rank constraint via matrix factorization [16–18], i.e., $\mathbf{C}_q = \mathbf{U}_q \mathbf{V}_q$, where $\mathbf{U}_q \in \mathbb{C}^{N \times r}$ and $\mathbf{V}_q \in \mathbb{C}^{r \times M}$ respectively span the spatial subspace and temporal subspace of $\mathbf{C}_q$.

Moreover, we can pre-estimate the temporal subspaces for the low-rank model prior to image reconstruction. Specifically, dictionaries can be generated via Bloch simulations that contain all possible magnetization evolutions, from which $\{\mathbf{V}_q\}$ can be estimated by the principled component analysis [15, 19]. As a consequence, the image reconstruction problem reduces to determining the spatial subspaces $\{\mathbf{U}_q\}$, i.e.,

$$\left\{\widehat{\mathbf{U}}_q\right\}_{q=1}^{N_s} = \arg \min_{\{\mathbf{U}_q\}} \sum_{c=1}^{N_c} \left\| \mathbf{d}_c - \Omega(\mathbf{F} \sum_{q=1}^{N_s} \mathbf{S}_{c,q} \mathbf{U}_q \widehat{\mathbf{V}}_q) \right\|_2^2, \quad (2)$$

where $\{\hat{\mathbf{V}}_q\}$ denote the pre-estimated temporal subspaces. After solving (2), the Casorati matrix associated with the contrast-weighted images can be formed, i.e., $\hat{\mathbf{C}}_q = \hat{\mathbf{U}}_q \hat{\mathbf{V}}_q$. Then we can estimate MR tissue parameters via dictionary based pattern matching as in the conventional approach.

2.2. Solution Algorithm

In this subsection, we describe a solution algorithm based on variable splitting (VS) and the alternating direction method of multipliers (ADMM) to solve (2). First, we apply the following VS scheme: $\mathbf{G}_q = \mathbf{U}_q \hat{\mathbf{V}}_q$ and $\mathbf{H}_c = \sum_{q=1}^{N_s} \mathbf{S}_{c,q} \mathbf{G}_q$, and form an equivalent constrained optimization problem as follows:

$$\min_{\mathbf{U}_q, \mathbf{G}_q, \mathbf{H}_c} \sum_{c=1}^{N_c} \|\mathbf{d}_c - \Omega(\mathbf{F}\mathbf{H}_c)\|_2^2, \quad \text{s.t.} \quad \mathbf{H}_c = \sum_{q=1}^{N_s} \mathbf{S}_{c,q} \mathbf{G}_q \text{ and } \mathbf{G}_q = \mathbf{U}_q \widehat{\mathbf{V}}_q. \tag{3}$$

Second, the augmented Lagrangian function associated with (3) is formed as follows:

$$L_{\mathscr{A}}(\mathbf{U}_q, \mathbf{G}_q, \mathbf{H}_c) = \sum_{c=1}^{N_c} \left\{ \|\mathbf{d}_c - \Omega(\mathbf{F}\mathbf{H}_c)\|_2^2 + \mathbf{Re}\left(< \mathbf{X}_c, \mathbf{H}_c - \sum_{q=1}^{N_s} \mathbf{S}_{c,q} \mathbf{G}_q > \right) + \frac{\mu_h}{2} \left\| \mathbf{H}_c - \sum_{q=1}^{N_s} \mathbf{S}_{c,q} \mathbf{G}_q \right\|_F^2 \right\}$$
$$+ \sum_{q=1}^{N_s} \left\{ \mathrm{Re}\left(< \mathbf{Y}_q, \mathbf{G}_q - \mathbf{U}_q \widehat{\mathbf{V}}_q > \right) + \frac{\mu_g}{2} \left\| \mathbf{G}_q - \mathbf{U}_q \widehat{\mathbf{V}}_q \right\|_F^2 \right\},$$

where $\{\mathbf{X}_c\}$ and $\{\mathbf{Y}_q\}$ are the Lagrangian multipliers, μ_g and μ_h are the penalty parameters, and **Re**(·) takes the real part of a complex number.

Third, we apply the ADMM algorithm to minimize $L_{\mathscr{A}}(\cdot)$. Here the algorithm consists of solving the following optimization problems:

$$\left\{ \mathbf{U}_q^{(k+1)} \right\}_{q=1}^{N_s} = \arg \min_{\mathbf{U}_q} L_{\mathscr{A}} \left(\mathbf{U}_q, \mathbf{G}_q^{(k)}, \mathbf{H}_c^{(k)} \right), \tag{4}$$

$$\left\{ \mathbf{G}_q^{(k+1)} \right\}_{q=1}^{N_s} = \arg \min_{\mathbf{G}_q} L_{\mathscr{A}} \left(\mathbf{U}_q^{(k+1)}, \mathbf{G}_q, \mathbf{H}_c^{(k)} \right), \tag{5}$$

$$\left\{\mathbf{H}_c^{(k+1)}\right\}_{c=1}^{N_c} = \arg\min_{\mathbf{H}_c} L_{\mathscr{A}}\left(\mathbf{U}_q^{(k+1)}, \mathbf{G}_q^{(k+1)}, \mathbf{H}_c\right), \quad (6)$$

and updating the Lagrangian multipliers:

$$\mathbf{X}_c^{(k+1)} = \mathbf{X}_c^{(k)} + \mu_h\left[\mathbf{H}_c^{(k+1)} - \sum_{q=1}^{N_s} \mathbf{S}_{c,q}\mathbf{G}_q^{(k+1)}\right],$$

$$\mathbf{Y}_q^{(k+1)} = \mathbf{Y}_q^{(k)} + \mu_g\left[\mathbf{G}_q^{(k+1)} - \mathbf{U}_q^{(k+1)}\widehat{\mathbf{V}}_q\right].$$

Next we describe the solutions to (4)–(6).

The optimization problem in (4) is separable with respect to each $\mathbf{U}_q$, and is equivalent to solving

$$\widehat{\mathbf{U}}_q^{(k+1)} = \arg\min_{\mathbf{U}_q} \left\|\mathbf{U}_q\widehat{\mathbf{V}}_q - \mathbf{G}_q - \frac{1}{\mu_g}\mathbf{Y}_q\right\|_2^2, \quad (7)$$

for $q = 1, \cdots, N_s$. Noting that $\widehat{\mathbf{V}}_q\widehat{\mathbf{V}}_q^H = \mathbf{I}$, the solution to (7) is given by

$$\widehat{\mathbf{U}}_q^{(k+1)} = \left(\mathbf{G}_q + \mathbf{Y}_q/\mu_g\right)\widehat{\mathbf{V}}_q^H.$$

The optimization problem in (5) can be written as

$$\min_{\{\mathbf{G}_q\}} \sum_{c=1}^{N_c} \frac{\mu_h}{2}\left\|\sum_{q=1}^{N_s}\mathbf{S}_{c,q}\mathbf{G}_q - \left(\mathbf{H}_c^{(k)} + \mathbf{X}_c^{(k)}/\mu_h\right)\right\|_F^2 + \sum_{q=1}^{N_s}\frac{\mu_g}{2}\left\|\mathbf{G}_q - \left(\mathbf{U}_q^{(k+1)}\widehat{\mathbf{V}}_q - \mathbf{Y}_{m,q}^{(k)}/\mu_g\right)\right\|_2^2,$$

(8)

for $q = 1, \cdots, N_s$. Further, (8) can be written into the following compact form:

$$\min_{\mathbf{G}} \frac{\mu_h}{2}\left\|\widetilde{\mathbf{S}}\mathbf{G} - \mathbf{Q}^{(k)}\right\|_F^2 + \frac{\mu_g}{2}\left\|\mathbf{G} - \mathbf{W}^{(k)}\right\|_F^2, \quad (9)$$

where

$$\mathbf{G} = \begin{bmatrix} \mathbf{G}_1 \\ \vdots \\ \mathbf{G}_{N_s} \end{bmatrix} \in \mathbb{C}^{NN_s \times M},$$

$$\widetilde{\mathbf{S}} = \begin{bmatrix} \mathbf{S}_{1,1} & \cdots & \mathbf{S}_{1,N_s} \\ \vdots & \ddots & \vdots \\ \mathbf{S}_{N_c,1} & \cdots & \mathbf{S}_{N_c,N_s} \end{bmatrix} \in \mathbb{C}^{NN_c \times NN_s},$$

$$\mathbf{Q}^{(k)} = \begin{bmatrix} \mathbf{H}_1^{(k)} + \mathbf{X}_1^{(k)}/\mu_h \\ \vdots \\ \mathbf{H}_{N_c}^{(k)} + \mathbf{X}_{N_c}^{(k)}/\mu_h \end{bmatrix} \in \mathbb{C}^{NN_c \times M},$$

and

$$\mathbf{W}^{(k)} = \begin{bmatrix} \mathbf{U}_1^{(k+1)}\widehat{\mathbf{V}}_1 - \mathbf{Y}_1^{(k)}/\mu_g \\ \vdots \\ \mathbf{U}_{N_s}^{(k+1)}\widehat{\mathbf{V}}_{N_s} - \mathbf{Y}_{N_s}^{(k)}/\mu_g \end{bmatrix} \in \mathbb{C}^{NN_s \times M}.$$

Eq. (9) is equivalent to solving

$$\left(\frac{\mu_h}{2}\widetilde{\mathbf{S}}^H\widetilde{\mathbf{S}} + \frac{\mu_g}{2}\mathbf{I}\right)\mathbf{G} = \frac{\mu_h}{2}\widetilde{\mathbf{S}}^H\mathbf{Q}^{(k)} + \frac{\mu_g}{2}\mathbf{W}^{(k)},$$

where $\mathbf{I}$ is the identity matrix. Noting that $\left(\frac{\mu_h}{2}\widetilde{\mathbf{S}}^H\widetilde{\mathbf{S}} + \frac{\mu_g}{2}\mathbf{I}\right)$ is a sparse matrix, the above equation can be efficiently solved by iterative algorithms (e.g., pre-conditioned conjugate gradient algorithm).

The optimization problem in (6) is separable with respect to each coil and is equivalent to solving

$$\mathbf{H}_c^{(k+1)} = \arg\min_{\mathbf{H}_c} \|\Omega(\mathbf{F}\mathbf{H}_c) - \mathbf{d}_c\|_2^2 + \frac{\mu_h}{2}\left\|\mathbf{H}_c - \sum_{q=1}^{N_s}\mathbf{S}_{c,q}\mathbf{G}_q^{(k+1)} + \mathbf{X}_c^{(k)}/\mu_h\right\|_F^2, \quad (10)$$

for $c = 1, \cdots, N_c$. Note that (10) is further separable with respect to each time instant, and is equivalent to solving

$$\left(\mathbf{F}_m^H\mathbf{F}_m+\frac{\mu_h}{2}\mathbf{I}\right)\mathbf{h}_{m,c}^{(k+1)}=\frac{\mu_h}{2}\left(\sum_{q=1}^{N_s}\mathbf{S}_{c,q}\mathbf{g}_{m,q}^{(k+1)}-\mathbf{x}_{m,c}^{(k)}/\mu_h\right)+\mathbf{F}_m^H\mathbf{d}_{m,c},$$

for $m = 1, \cdots, M$, where $\mathbf{h}_{m,c}$, $\mathbf{g}_{m,q}$, $\mathbf{x}_{m,c}$ are the mth columns of $\mathbf{H}_c$, $\mathbf{G}_q$, and $\mathbf{X}_c$, respectively. Noting that the coefficient matrix $\left(\mathbf{F}_m^H\mathbf{F}_m+\frac{\mu_h}{2}\mathbf{I}\right)$ has a block Toeplitz structure, the above equation can be solved by a number of efficient numerical solvers (e.g., hierarchically semiseparable solver [20]).

3. RESULTS

Representative results from numerical experiments are shown to illustrate the performance of the proposed method. A numerical phantom based on the BrainWeb database [21] was built, in which three imaging slices (containing T_1, T_2, and spin density maps) were taken with a distance of 35 mm apart. We simulated the MRF experiments using an inversion recovery fast imaging with steady state free precession (IR-FISP) pulse sequence with the same acquisition parameters as in [22], and synthesized the contrast-weighted images with the extended phase graph formalism [23]. We generated coil sensitivity maps associated with a 32 channel receiver head coil using a Biot-Savart calculator. A multiband RF pulse was used to excite three imaging slices (i.e., MB = 3), and the t-blipped SMS-MRF was simulated by adding 120° phase difference between the three slices, with an increment of 120° phase across all three slices from one TR to the next. We used the same set of spiral trajectories as in [22], which consists of 48 spiral interleaves. A single spiral interleave was acquired for each TR such that the in-plane acceleration is AF = 48. The **k**-space data were synthesized with the nonuniform fast Fourier transform [24], and the length of the MRF acquisition was set as $M = 500$.

We perform image reconstruction using the conventional approach in [7] and the proposed method. Figs. 1, 2, and 3 respectively show the reconstructed T_1, T_2 and spin density maps, along with the voxelwise normalized error maps. Here we also calculate the overall normalized root-mean-square error (NRMSE) for the reconstructed parameter maps, defined as NRMSE = $\|\boldsymbol{\theta}-\hat{\boldsymbol{\theta}}\|_2/\|\boldsymbol{\theta}\|_2$. Here $\boldsymbol{\theta}$ and $\hat{\boldsymbol{\theta}}$ respectively denote the true parameter and reconstructed parameter. As can be seen, the proposed method yields more accurate T_1, T_2, and spin density maps than the conventional approach, although the improvement is more pronounced for the T_2 and spin density maps. Qualitatively, the proposed method reduces the ringing and shading-like artifacts appearing in the T_2 and spin maps from the conventional approach. Clearly, due to the high slice acceleration (i.e., MB = 3) and in-plane acceleration (i.e., AF = 48), the conventional approach that simply combines the slice SENSE with dictionary matching could not fully resolve alising artifacts. In contrast, the proposed method, which integrates the advanced low-dimensional image model with parallel imaging, leads to substantial performance improvement.

4. CONCLUSION

In this paper, we present a new image reconstruction method based on low-rank and subspace modeling for SMS-MRF. With the proposed model, the image reconstruction problem is formulated as a convex optimization problem, for which a numerical algorithm based on variable splitting and the alternating direction method of multipliers is described. The performance of the proposed method is evaluated by numerical experiments, and the results demonstrate the improved accuracy provided by the proposed method.

In the future work, it is worth evaluating the performance of the proposed method with in vivo experiments. Moreover, note that the proposed method provides a general image reconstruction framework for SMS-MRF, for which a number of extensions can be performed. For example, the proposed method can incorporate with some specialized blipped spiral trajectory [25], and/or more flexible signal excitation scheme [9] for SMS-MRF data acquisitions. Additionally, we can integrate the proposed low-rank and subspace model with sparsity constraint [26], which could potentially lead to improved performance, although this will increase the computational cost.

Acknowledgments

This work was supported in part by research grants: NIH-R01-EB017219, NIH-F32-EB024381, NIH-R01-EB017337, NIH-R01-NS089212, NIH-P41-EB015896, NIH-U01-MH093765, and NIH-R24-MH106096.

References

1. Tofts, P. Quantitative MRI of the brain: Measuring changes caused by disease. Wiley; New York, NY, USA: 2004.
2. Ma D, Gulani V, Seiberlich N, Liu K, Sunshine JL, Duerk JL, Griswold MA. Magnetic resonance fingerprinting. Nature. 2013; 495:187–192. [PubMed: 23486058]
3. Breuer FA, Blaimer M, Heidemann RM, Mueller MF, Griswold MA, Jakob PM. Controlled aliasing in parallel imaging results in higher acceleration (CAIPIRINHA) for multi-slice imaging. Magn Reson Med. 2005; 53:684–691. [PubMed: 15723404]
4. Breuer FA, Blaimer M, Heidemann RM, Mueller MF, Griswold MA, Jakob PM. Multiplexed echo planar imaging for sub-second whole brain FMRI and fast diffusion imaging. PLoS One. 2010; 5:e15710. [PubMed: 21187930]
5. Setsompop K, Gagoski BA, Polimeni JR, Witzel T, Wedeen VJ, Wald LL. Blipped-controlled aliasing in parallel imaging for simultaneous multislice echo planar imaging with reduced g-factor penalty. Magn Reson Med. 2012; 67:1210–1224. [PubMed: 21858868]
6. Feinberg DA, Setsompop K. Ultra-fast MRI of the human brain with simultaneous multi-slice imaging. J Magn Reson. 2013; 229:90–100. [PubMed: 23473893]
7. Ye H, Ma D, Jiang Y, Cauley SF, Du Y, Wald LL, Griswold MA, Setsompop K. Accelerating magnetic resonance fingerprinting (MRF) using t-blipped simultaneous multislice (SMS) acquisition. Magn Reson Med. 2016; 75:2078–2085. [PubMed: 26059430]
8. Ye H, Cauley SF, Gagoski B, Bilgic B, Ma D, Jiang Y, Du Y, Griswold MA, Wald LL, Setsompop K. Simultaneous multislice magnetic resonance fingerprinting (SMS-MRF) with direct-spiral slice-grappa (ds-SG) reconstruction. Magn Reson Med. 2017 in press.
9. Jiang Y, Ma D, Bhat H, Ye H, Cauley SF, Wald LL, Setsompop K, Griswold MA. Use of pattern recognition for unaliasing simultaneously acquired slices in simultaneous multislice MR fingerprinting. Magn Reson Med. 2017 in press.

10. Zhao B, Setsompop K, Adalsteinsson E, Gagoski B, Ye H, Ma D, Jiang Y, Grant PE, Griswold MA, Wald LL. Improved magnetic resonance fingerprinting reconstruction with low-rank and subspace modeling. Magn Reson Med. in press.
11. Afonso MV, Bioucas-Dias JM, Figueiredo MAT. Fast image recovery using variable splitting and constrained optimization. IEEE Trans Image Process. 2010; 19:2345–2356. [PubMed: 20378469]
12. Ramani S, Fessler JA. Parallel MR image reconstruction using augmented Lagrangian methods. IEEE Trans Med Imag. 2011; 30:694–706.
13. Zhao B, Setsompop K, Ye H, Cauley S, Wald LL. Maximum likelihood reconstruction for magnetic resonance fingerprinting. IEEE Trans Med Imag. 2016; 35(8):1812–1823.
14. Boyd S, Parikh N, Chu E, Peleato B, Eckstein J. Distributed optimization and statistical learning via the alternating direction method of multipliers. Found Trends Mach Learn. 2011; 3:1–122.
15. Liang Z-P. Spatiotemporal imaging with partially separable functions. Proc IEEE Int Symp Biomed Imaging. 2007:905–909.
16. Haldar JP, Liang Z-P. Spatiotemporal imaging with partially separable functions: A matrix recovery approach. Proc IEEE Int Symp Biomed Imaging. 2010:716–719.
17. Zhao B, Haldar JP, Brinegar C, Liang Z-P. Low rank matrix recovery for real-time cardiac MRI. Proc IEEE Int Symp Biomed Imaging. 2010:996–999.
18. Zhao B, Haldar JP, Christodoulou AG, Liang ZP. Image reconstruction from highly undersampled (**k**, *t*)-space data with joint partial separability and sparsity constraints. IEEE Trans Med Imag. 2012; 31:1809–1820.
19. Sen Gupta A, Liang Z-P. Dynamic imaging by temporal modeling with principle component analysis. Proc Int Symp Magn Reson Med. 2001:10.
20. Cauley SF, Xi Y, Bilgic B, Xia J, Adalsteinsson E, Balakrishnan V, Wald LL, Setsompop K. Fast reconstruction for multichannel compressed sensing using a hierarchically semiseparable solver. Magn Reson Med. 2015; 73:1034–1040. [PubMed: 24639238]
21. Collins DL, Zijdenbos AP, Kollokian V, Sled JG, Kabani NJ, Holmes CJ, Evans AC. Design and construction of a realistic digital brain phantom. IEEE Trans Med Imag. 1998; 17:463–468.
22. Jiang Y, Ma D, Seiberlich N, Gulani V, Griswold MA. MR fingerprinting using fast imaging with steady state precession (FISP) with spiral readout. Magn Reson Med. 2015; 74:1621–1631. [PubMed: 25491018]
23. Hennig J. Multiecho imaging sequences with low refocusing flip angles. J Magn Reson. 1988; 78:397–407.
24. Fessler JA, Sutton BP. Nonuniform fast fourier transforms using min-max interpolation. IEEE Trans Signal Process. 2003; 51:560–574.
25. Zahneisen B, Poser BA, Ernst T, Stenger AV. Simultaneous Multi-Slice fMRI using spiral trajectories. NeuroImage. 2014; 92:8–18. [PubMed: 24518259]
26. Zhao B, Lu W, Hitchens TK, Lam F, Ho C, Liang ZP. Accelerated MR parameter mapping with low-rank and sparsity constraints. Magn Reson Med. 2015; 74:489–498. [PubMed: 25163720]

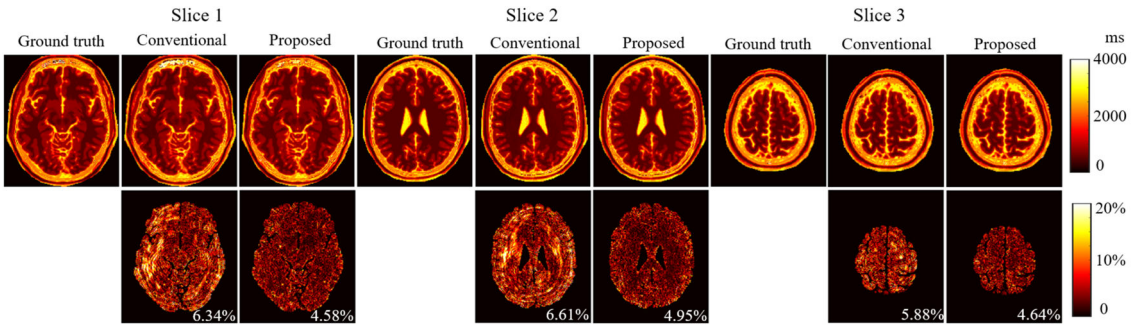

Fig. 1.

Reconstructed T_1 maps and associated error maps for SMS-MRF with SMS = 3 using the conventional approach and the proposed method. Note that the overall error is labeled at lower right corner of each error map, and that the skull and scalp were removed from each error map.

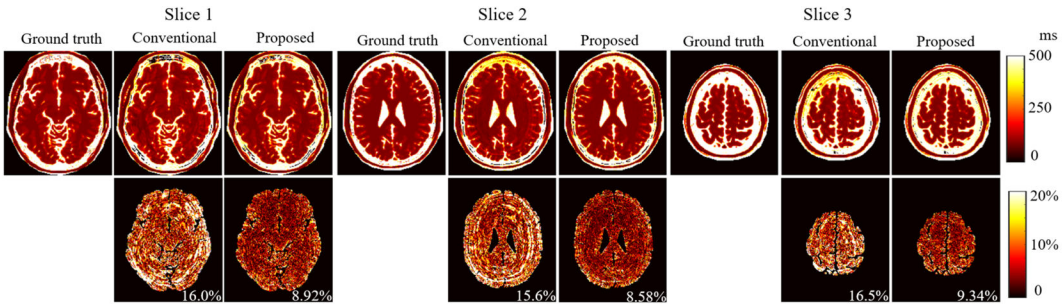

Fig. 2.

Reconstructed T_2 maps and associated error maps for SMS-MRF with SMS = 3 using the conventional approach and the proposed method. Note that the overall error is labeled at lower right corner of each error map, and that the skull and scalp were removed from each error map.

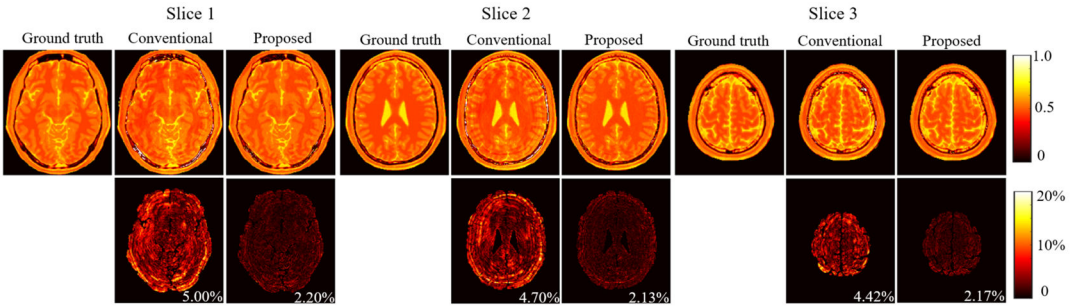

Fig. 3.

Reconstructed spin density maps and associated error maps for SMS-MRF with SMS = 3 using the conventional approach and the proposed method. Note that the overall error is labeled at lower right corner of each error map, and that the skull and scalp were removed from each error map.